Investigation of Batch Fluidized-Bed Drying by Mathematical Modeling, CFD Simulation and ECT Measurement

H. G. Wang and W. Q. Yang
School of Electrical and Electronic Engineering, The University of Manchester, PO Box 88, Manchester M60 1QD, U.K.

P. Senior and R. S. Raghavan
School of Chemical Engineering and Analytical Science, The University of Manchester, PO Box 88, Manchester M60 1QD, U.K.

S. R. Duncan
Dept. of Engineering Science, University of Oxford, Parks Road, Oxford OX1 3PJ, U.K.

DOI 10.1002/aic.11406
Published online December 27, 2007 in Wiley InterScience (www.interscience.wiley.com).

Mathematical modeling, computational fluid dynamics (CFD) analysis and electrical capacitance tomography (ECT) is used to develop an understanding of batch fluidized-bed drying, which is a complex air-solids, multiphase process. The mathematical model is based on a three-phase theory that describes the mass-and heat-transfer between the air and solids phases. The CFD model is based on a two-fluid model (TFM) approach, in which both phases are considered to be continuous and fully interpenetrating. The hydrodynamic parameters used to model the heat-and mass-transfer between the two phases are determined by a correlation approach, and the estimated parameters are incorporated into a user defined function (UDF) in FLUENT. The moisture diffusion in the air and solids phases is simulated using the user defined scalar (UDS) transport equation in the software package. ECT is used for the online solids concentration and moisture measurement, based on dynamic calibration. Comprehensive comparisons between results from mathematical modeling, CFD simulation and ECT measurement are presented, and are validated using experiment results. Online measurement of moisture content is compared with a static calibration. The mathematical model, CFD and ECT presented are being integrated into an online process control system for a batch fluidized-bed drying application in the pharmaceutical industry. © 2007 American Institute of Chemical Engineers *AIChE J,* 54: 427–444, 2008
Keywords: fluidized-bed drying, mathematical model, two-fluid model, ECT, moisture measurement, dynamical calibration, heat-and mass-transfer

Introduction

Compared to conventional packed-bed or moving-bed dryers, fluidized-bed dryers have a number of attractive features, such as high-efficient air-solids contact due to good mixing

Correspondence concerning this article should be addressed to H. Wang at haigang.wang@manchester.ac.uk.

and uniformity,[1] extremely rapid heat-transfer rate, and relatively short drying times. Because of these advantages, fluidized-bed drying is widely used in the pharmaceutical and other chemical process industry either as a batch or continuous process.[2]

The drying process is mainly controlled by two parameters: (1) the moisture content, and (2) the temperature of product. Precise measurement of these two parameters in each of the phases present inside a dryer is important for both process design and product quality control. The research carried out to investigate the drying processes in fluidized-bed dryers can be classified into three categories: (1) mathematical modeling; (2) computational fluid dynamics (CFD) simulation, and (3) experimental measurement. While CFD simulations on spouted bed drying[3,4] and pneumatic drying[5,6] have been reported, this article will extend these studies by using CFD to model the heat-and mass-transfer within fluidized-bed drying, and compare these simulations with measurements taken by electrical capacitance tomography (ECT). CFD simulation is very time-consuming, because the air-particle flow in a fluidized-bed dryer is complex, primarily because it is a two-phase flow.[2,7] As a result, the CFD simulations are carried out offline and are primarily used for process optimization.

Mathematical modeling is fast, and can be used online, and there are many mathematical models for continuous[8,9,10,11] and batch[12,13,14,15] fluidized-beds drying. Most of these models are based on the three-phase theory.[16,17]

Compared with temperature measurement, online measurement of moisture content is challenging in a fluidized-bed dryer. Currently, the moisture content of pharmaceutical granules in a fluidized-bed dryer is measured indirectly by taking a sample of the bed, whose moisture is then measured offline. In some processes, it is necessary to shut down the fluidized-bed dryer while taking the sample for measurement, which leads to the cooling down of the material in the bed, and if drying is found to be incomplete, the bed may need to be reheated before the drying process can be completed, resulting in energy wastage and low-operating efficiency. Reliable, online measurement of moisture content would overcome these problems, and some online measurement tools have been reported, including near infrared spectroscopy (NIR),[18,19] microwave,[20] capacitance probe,[21] and nuclear methods.[22] The microwave method has been successfully used for online measurement of moisture, but its sensing depth is limited. Some examples of moisture measurement by microwave are conveyors, filtration, palletizing and sintering processes. The nuclear method is used for measuring highly conductive materials, such as coke and magnetite, but requires careful shielding is necessary to avoid radiation hazards. Up to now, there is no efficient tool available for online measurement of moisture content in fluidized-bed dryers and as a result, the operation and control of fluidized-bed dryer systems has lagged behind other sectors in the pharmaceutical industry.[23]

In this article, a new approach based on mathematical modeling, CFD simulation and ECT measurement is presented. A granular drying process has been investigated using a dedicated mathematical model, and a commercial CFD package, FLUENT v6.1. The moisture content is measured online by ECT to provide dynamic calibration. The aim of this research is to investigate process modeling and control of fluidized-bed drying, optimize operation parameters, increase operation efficiency and improve product quality. The objectives of this study are: (1) to understand the mass-and heat-transfer phenomena in fluidized-bed drying processes, (2) to provide an online model for controlling the fluidized-bed drying processes, (3) to provide an online measurement of moisture content without the need to shut down the fluidized-bed dryer, and (4) to evaluate the accuracy of online measurement of moisture content using an offline tool.

Models

Mathematical model

The mathematical model used in this research is based on the three-phase theory, which is used to describe the mass-and heat-transfer between the air and solids phases in a batch fluidized-bed dryer.[15] In the model, it is assumed that the dilute phase (i.e., bubbles) is a plug flow, while the interstitial air and the solid particles are considered as being perfectly mixed. The thermal conductivity of wet particles is modeled using a serial and parallel circuit. The moisture content of the saturated drying medium at the surface of the wet solid particles is a function of temperature and moisture content of particles and can be expressed as[10]

$$X_s^* = \phi_1(T_s)\phi_2(X_s) \tag{1}$$

where the functions can be computed from a tension curve of the moisture, and the absorption character of the solids moisture system. The approximations are

$$\phi_1(T_s) = 0.622\frac{p_w}{p_o - p_w} \tag{2}$$

$$\phi_2(X_s) = \begin{cases} 1 & X_s > X_c \\ X_p^n/(X_p^n + K) & X_s < X_c \end{cases} \tag{3}$$

where

$$p_w = 1.0 \times 10^5 \exp(13.869 - 5173/T_s) \tag{4}$$

During the drying process, the thermal conductivity of the solids phase change due to the decrease of moisture content. Both the mathematical model and CFD simulation use the same formula for thermal conductivity of wet granule given in the reference article.[15]

CFD model

CFD is one of the most productive numerical methods. It can facilitate the process and product development cycles and achieve optimal control. A CFD method has been used to simulate a drying process in a spouted bed dryer,[3,4] and steady pneumatic drying.[5,6] The CFD model used in this research is based on the two-fluid model (TFM), which in turn, is based on the kinetic theory for granular flows.[24,25] In this approach, the usual thermodynamic temperature is replaced by the granular-flow temperature (θ). The viscosity, stress and pressure of solids are a function of the granular temperature, which varies with time and position in a fluidized bed.[7] Table 1 lists the TFM mass, momentum, energy conservation equations for both phases in the Cartesian (x, y, z) coordinate system.

Table 1. TFM Mass, Momentum and Thermal Energy Conservation Equations in Vector Form

Continuous
Air phase

$$\frac{\partial \varepsilon_g \rho_g}{\partial t} + \nabla \cdot (\varepsilon_g \rho_g \vec{V}_g) = \dot{m} \quad (5)$$

Solids phase

$$\frac{\partial \varepsilon_s \rho_s}{\partial t} + \nabla \cdot (\varepsilon_s \rho_s \vec{V}_s) = -\dot{m} \quad (6)$$

Momentum
Fluid phase

$$\frac{\partial}{\partial t}(\varepsilon_g \rho_g \vec{V}_g) + \nabla \cdot (\varepsilon_g \rho_g \vec{V}_g \vec{V}_g) = -\varepsilon_g \nabla p + \nabla \cdot \bar{\bar{\tau}}_g + \varepsilon_g \rho_g g - \beta(\vec{V}_g - \vec{V}_s) \quad (7)$$

Solids phase

$$\frac{\partial}{\partial t}(\varepsilon_s \rho_s \vec{V}_s) + \nabla \cdot (\varepsilon_s \rho_s \vec{V}_s \vec{V}_s) = -\nabla p_s - \varepsilon_s \nabla p + \nabla \cdot \bar{\bar{\tau}}_s + \varepsilon_s \rho_s g - \beta(\vec{V}_s - \vec{V}_g) \quad (8)$$

Thermal energy
Fluid phase

$$\frac{\partial}{\partial t}(\varepsilon_g \rho_g h_g) + \nabla \cdot (\varepsilon_g \rho_g V_g h_g) = -\nabla \cdot \varepsilon_g \lambda_g \nabla T_g + h_t(T_s - T_s) + \tau_g \cdot \nabla \cdot V_g + \varepsilon_g \left[\frac{\partial}{\partial t} p + V_g \nabla p\right] + \beta(V_g - V_s)V_g + \Delta H_{vap} \dot{m} \quad (9)$$

Solids phase

$$\frac{\partial}{\partial t}(\varepsilon_s \rho_s h_s) + \nabla \cdot (\varepsilon_s \rho_s V_s h_s) = -\nabla \cdot \varepsilon_s \lambda_s \nabla T_s + h_t(T_g - T_s) + \tau_s \cdot \nabla \cdot V_s + \varepsilon_s \left[\frac{\partial}{\partial t} p + V_s \nabla p\right] + \beta(V_g - V_s)V_s - \Delta H_{vap} \dot{m} \quad (10)$$

This model requires additional constitutive equations to describe the air and solids stress tensors $\bar{\bar{\tau}}_g$ and $\bar{\bar{\tau}}_s$, air-particle interphase drag coefficient β, solids pressure p_s and transfer rate between the two phases. Ding and Gidaspow,[25] Gidaspow[26,27] and Lun[24] reported the use of the kinetic theory for modeling granular flows. The governing equation for the temperature of a granular flow (θ) is given by

$$\frac{3}{2}\left[\frac{\partial}{\partial t}(\varepsilon_s \rho_s \theta) + \nabla \cdot (\varepsilon_s \rho_s \theta \vec{V}_s)\right] = (-P_s I + \bar{\bar{\tau}}_s) : \nabla \vec{V}_s + \nabla \cdot (k_s \nabla \theta) - \gamma_s + \phi_s \quad (11)$$

The terms on the righthand side of Eq. 7 can be found in the reference article[25], while the stress tensor of solids, and the pressure of the solids phase can be derived from the granule kinetic temperature.[25] The convective heat-and mass-transfer rate between the air and solids phases are

$$\dot{q} = N_p A_{p,s} h_t (T_g - T_p) \quad (12)$$

$$\dot{m} = N_p A_{p,s} h_s (X_s^* - X_g) \quad (13)$$

where, N_p is the number of particles per volume $A_{p,s}$ is the external surface area of the particle, and h_t and h_s are the local values of the transfer coefficient, which can be determined by Gunn's relationship[28]

$$Nu = (7 - 10\varepsilon_f + 5\varepsilon_f^2)(1 + 0.7Re_p^{0.2}Pr^{1/3}) + (1.33 - 2.4\varepsilon_f + 1.2\varepsilon_f^2)Re_p^{0.7}Pr^{1/3} \quad (14)$$

$$Sch = (7 - 10\varepsilon_f + 5\varepsilon_f^2)(1 + 0.7Re_p^{0.2}Sc^{1/3}) + (1.33 - 2.4\varepsilon_f + 1.2\varepsilon_f^2)Re_p^{0.7}Sc^{1/3} \quad (15)$$

where ε_f is the voidage fraction of air, Re_p is the Reynolds number, Pr is the Prandtl number, Sc is the Schmidit number, Nu is the Nusselt number, Sch is the Scherwood number

$$Nu = \frac{h_t d_p}{k_g}, \quad Sch = \frac{h_s d_p}{D_v}, \quad Re_p = \frac{\rho_g U_0 d_p}{\mu_g}, \quad Pr = \frac{c_{pg}}{\rho_g k_g}, \quad Sc = \frac{\mu_f}{\rho D_v} \quad (16)$$

which are all dimensionless parameters. In Eqs. 9 and 10, the latent heat due to vaporization of water is given by[8]

$$\Delta H = 3168.0 - 2.4364T \quad (17)$$

In Eq. 13 X_s^*, is the moisture content of the saturated drying medium at the surface of the wet solid particle, which is given in Eq. 1.

To model the moisture transfer in the fluid and solids phase, a user define scale (UDS) has been added to the FLUENT model, which can be written as

$$\frac{\partial}{\partial t}(\varepsilon_g \rho_g Y_v) + \nabla \cdot (\varepsilon_g \rho_g V_g Y_v) = \nabla \cdot (D_v \rho_v \varepsilon_g \nabla Y_v) + \dot{m} \quad (18)$$

$$\frac{\partial}{\partial t}(\varepsilon_s \rho_s X_s) + \nabla \cdot (\varepsilon_s \rho_s V_s X_s) = \nabla \cdot (D_v \rho_s \varepsilon_s \nabla X_v) - \dot{m} \quad (19)$$

Equations 12–19 are added to FLUENT as complied executable code, by means of UDF and UDS programming, expanding its capability.

Due to the change of the water content of the wet granule during the drying process, the density of the solids phase will change, and is defined as

$$\rho_s = \rho_w \cdot X_s + \rho_p \quad (20)$$

During the constant-rate period the granular diameter shrinks due to evaporation from the outer surface to the surrounding air, and is given by

$$d_p = d_{p0} - \sqrt[3]{\frac{6}{\pi}\frac{\rho_s}{\rho_l}(X_{s0} - (X_s - X_{cr}))} \quad (21)$$

where, the subscript means the initial condition.

Equations 5–21, with the boundary and initial conditions can be solved numerically using FLUENT, which uses a

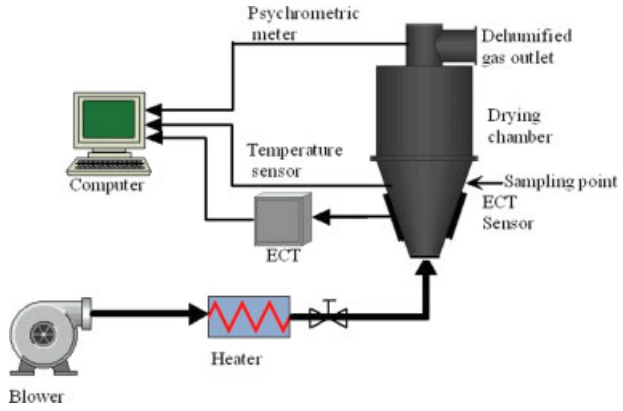

Figure 1. Fluidized-bed dryer and instrumentation.

[Color figure can be viewed in the online issue, which is available at www.interscience.wiley.com.]

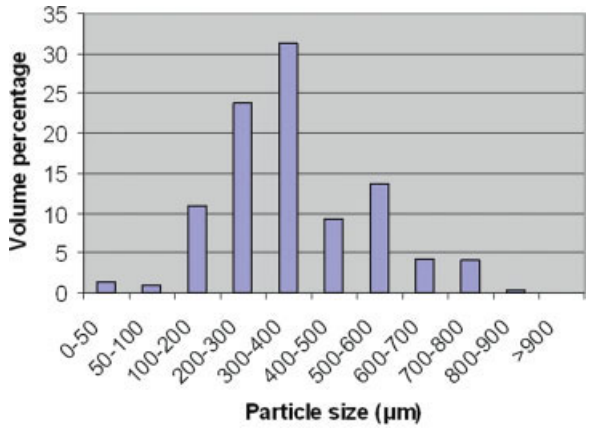

Figure 2. Particle-size distribution.

[Color figure can be viewed in the online issue, which is available at www.interscience.wiley.com.]

control-volume-based technique to convert the governing Eqs. 5–11, 18–19 to algebraic equations on each finite cell. The wall of the fluidized bed is treated as nonslip boundary for the air phase, that is, the velocity of the air phase is set to zero at the wall. For the solids phase the free-slip condition is assumed, that is, there is no hindrance in the downward or upward velocity of the particles when they are near the wall. The thermoboundary at the walls is treated as the adiabatic condition, that is, there is no heat flux between the fluid and wall. The granular temperature of the solids-phase at the wall was given in[29]. At the outlet, the pressure of ambient atmosphere and continuous mass fluxes of both air and solids are assumed. Initially, the bed is operated at incipient fluidization conditions, with a superficial air velocity above the minimum fluidization velocity. More details on the solids-phase boundary are given by Sinclair and Jackson.[30] To validate the CFD results, images are reconstructed from ECT measurements using the same grid dimensions as the CFD simulation.

Fluidized- bed dryer setup and ECT measurement

A laboratory scale M501 fluidized-bed dryer with an ECT sensor and instrumentation for the test is shown in Figure 1. The detailed parameters, experimental conditions and physical properties of particles are listed in Table 2. The frame of the ECT sensor is the wall of the fluidized bed, and the ECT sensor is enclosed by an earthed shielding to eliminate external interference. There are 12 electrodes (4 cm long and 2.5 cm wide in average) around a cross section of the fluidized bed. The measurement region encompasses a conical part between 3 and 10 cm above the distributor. Therefore, each pixel in an ECT image represents an axial average over the rectangle measurement volume. The ECT system used is based on AC capacitance measuring circuits with a data acquisition rate of 120 frames per second.[31]

To improve the image quality and measurement accuracy, an optional iteration method based on the Landweber method is used for reconstructing images.[32] An HB43 moisture meter from Mettler-Toledo was used as a reference measurement to determine the moisture content during the drying process.

For preparation of the wet granule, water droplets were sprayed to and combined with the dry material in a low-speed food mixer for 10 min. The granulation product was then sieved through a 1.5 mm screen to remove large particles resulting from the agglomeration of wet fine particles. The maximum amount of wet granular material that could be produced by the granulator was 2.0 kg, and the quantities of dry granule and water needed are 0.95 kg. The particle-size distribution, determined using a Malvern particle-size analyzer (Mastersizer 2000), is shown in Figure 2. The mass average diameter is 380 μm. The bulk density of the particle is around 760 $kg \cdot m^{-3}$, which is typical of Geldart B type particles. To determine the moisture content of the granule by HB43 during a drying process, a sampling point was made in the conical part of fluidized bed as shown in Figure 1, so that a sample of approximately 2.5 g could be taken from the fluidized bed and used to determine the moisture content of the granules.

Table 2. Experiment Conditions

Experiment Unit	Operating Condition
Column	Cross section in cylinder part: diameter – 16 cm, height – 40 cm Cross section in conical part: bottom diameter – 10 cm, top diameter – 16 cm, height – 10 cm
Distributor	Wire mesh with 20 μm holes in mesh
Fluidizing air	Air at ambient condition with temperature in a range of 15–85°C
Superficial air velocity	Operating in a range of 0.2–2.4 m/s
Material	Semolina: density – 760 kg/m^3, average particle diameter – 380 μm
ECT system	Single plane, 12 electrodes, AC-based ECT
Experimental duration	80 minutes

Table 3. Mesh Size Information

Mesh No.	Cell	Face	Node
1	630	1319	690
2	1062	2201	1140
3	1584	3262	1679
4	2520	5158	2639
5	4440	9037	4598
6	6292	12771	6490
7	9845	19924	10080

To obtain the drying curve, air at ambient condition is supplied by a centrifugal fan as shown in Figure 1, and then heated by an electrical heater. The hot air passes through a distributor to achieve more uniform flow, which then enters the conical chamber. The air temperature and velocity can be controlled by a PC up to 200°C and 3.0 m/s with an accuracy of ± 1.0°C and $\pm 5\ \mathrm{cm \cdot s^{-1}}$, respectively. The air used to fluidize the bed was heated to an inlet temperature of 65°C, as measured at a point just below the air distributor. The superficial air velocity, defined as the average velocity across the inlet to the conical section can be varied in the range of 0.2 to 2.4 $\mathrm{m \cdot s^{-1}}$, due to the change of the bulk density during drying process. These operation conditions correspond to those used in the pharmaceutical industry for the drying of wet granule. The bulk temperature was measured using PT1000 thermocouples, as shown in Figure 1. Every 4 or 5 min, samples of approximately 2.5 g were taken, and their moisture content measured, so that the drying rate could be determined and used to validate the simulation and the ECT measurement results.

Results and Analysis

Grid-size sensitivity analysis

The spatial resolution is an importance parameter in CFD simulation. The grid size is the main parameter involving this problem,[33,34] because it plays an important role in the numerical resolution, and also determines how much computational effort is needed. Therefore, to investigate the effect of grid size on resolution, simulation was repeated using different number of cells, as listed in Table 3. The number of cells, and the point for each set of mesh are also listed in Table 3. All the simulations used the first-order unwinding scheme to solve Eqs. 5–11, with the same boundary and initial conditions for all the mesh sets as listed in Table 3.

Figure 3 shows the solids concentration, vapor fraction in the air phase and the temperature of the solids phase in t = 5 s for different mesh sets. It can be seen that the predicted bubble shape and boundary begin to converge to the same shape with the increase in grid size, especially after the number of grids goes up to 2,520. The same trends can be seen from the distribution profiles of vapor fraction and the solids temperature in Figure 3.

Figure 4 shows the average solids concentration β_s, solids temperature T_p, *Sch* number and mass-transfer coefficient curves, which vary with the drying time. From these curves, it is clear that the numerical simulation is sensitive to the grid size when the number of grids is less than 2,520. When the number increases to 2,520, however, the simulation results show relatively low-sensitivity to the grid size, even though the numerical precision slightly increases with a smaller mesh size. From this simulation, the mesh of 4 to 7 nearly gives the same result. In this article, the mesh sets of 4 to 7 with a fine mesh, and 1 to 3 with a coarse mesh were used. In this way, the effect of grid size on numerical solution can be evaluated. The effect of grid size on the average solids concentration at a different position in the fluidized-bed dryer, heat-and mass-transfer, power spectrum structure will be given in the next section.

From the average parameters profile as shown in Figure 4, especially for the fine mesh, it indicates that there is still some room for improvement of numerical resolution. However, further increases in numerical resolution were not

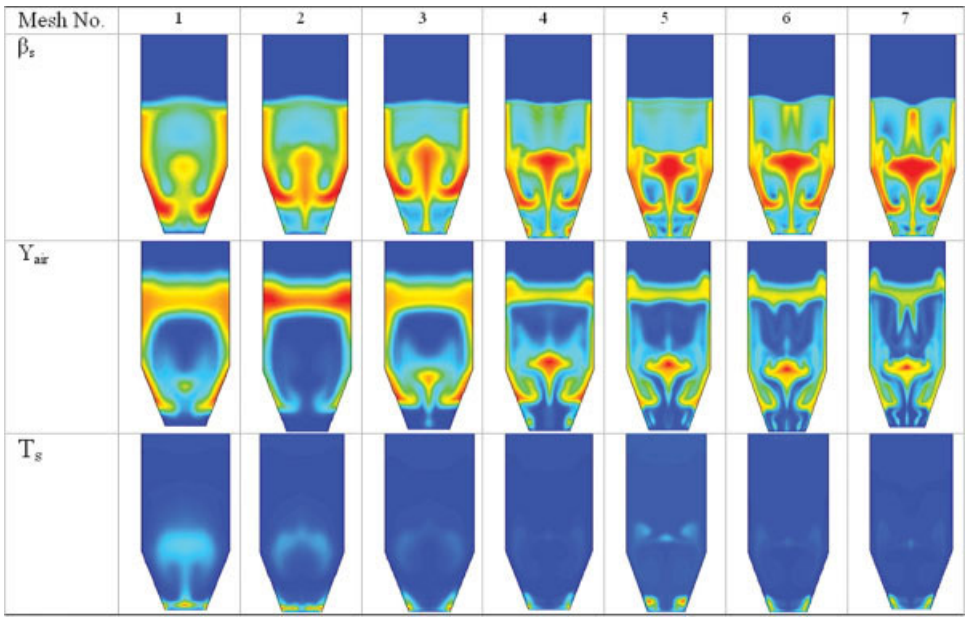

Figure 3. Instantaneous parameter distributions obtained by CFD simulation with different grid size.

[Color figure can be viewed in the online issue, which is available at www.interscience.wiley.com.]

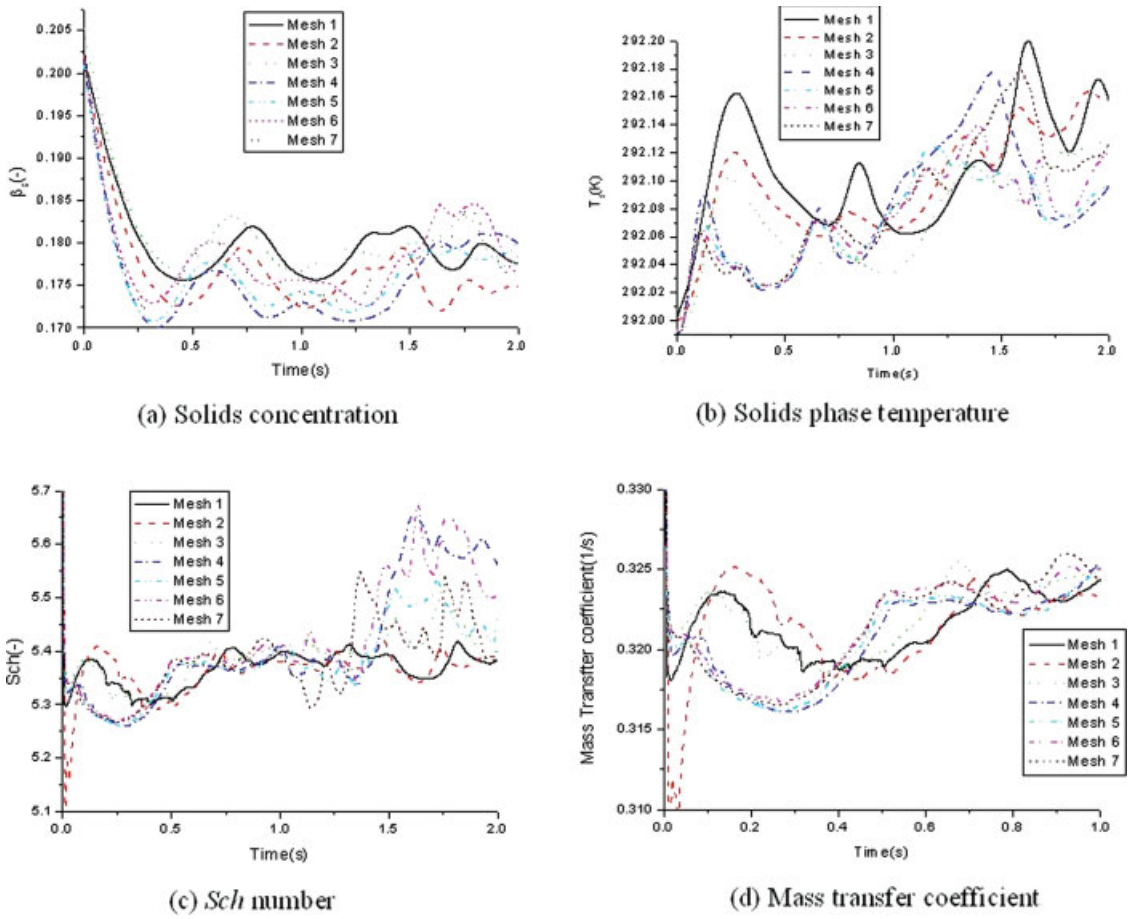

Figure 4. Average parameters distribution profile with different grid size.

[Color figure can be viewed in the online issue, which is available at www.interscience.wiley.com.]

pursued, because of the dramatic increase in computational demand. The demand of CPU time based on Intel Core CPU T7200 for 0.1 s simulation of drying is listed in Table 4. Considering the CPU time and spatial resolution, in this research, the simulation is based on the grid size of 2,520.

Measurement of solids concentration by CFD simulation and ECT

Figure 5 shows the simulated instantaneous particle concentration in the x–z sliced planes at difference drying time. The results for particle diameters of 600 μm and 380 μm are shown and in both cases, the fluidization air velocity is 2.0 $m \cdot s^{-1}$. As can been from the particle concentration profiles (Figure 5), in both sets of results, air bubbles were created near the bottom corners of the bed at $t = 1.0$ s, and these bubbles move up and grow after time $t = 5$ s. The coalescence of bubbles can also be seen clearly from these CFD simulation results. This coalescence behavior is consistent with the explanation by Clift and Grace.[35] As a result of coalescence near the top of the bed, bubbles in this region are larger than those near the bottom. At the top of the bed, the size of the bubble is comparable with the diameter of the bed. The bubble diameter in these two cases is nearly the same, because the particles belong to Geldart B type.

Figure 6 shows the effect of grid size on the average solids concentration in two positions in the bed, namely z = 15 cm, and z = 5 cm. It can be seen that with the increase in mesh size as listed in Table 3, the concentration profiles in different positions begin to converge to a stable value. From the simulation results, after the gird size increases to 2,520, the simulation becomes less sensitive to the mesh size, which agrees well with the sensitivity analysis in the first section.

Figure 7 shows the solids concentration by ECT measurement, where the left pictures are the solid concentrations at x-y cross-section, and the right curves are the time-average profile in radial direction with different superficial air velocity. The solids concentration in these cross-sections is the average value between $z = 3$ cm and $z = 10$ cm above the air distributor. The ECT measurement results show that the solids concentration decreases with the increase of fluidization air velocity, indicating that the bubble diameter increases with the excess air velocity U_0–U_{mf}. The measurement results agree well with the Geldart theory,[36] although it is difficult to compare the instantaneous distribution profiles generated by ECT measurement with those from the CFD simulation due to the dynamic movement of two-phase consisting of the air and solids in the fluidized bed. However, the time-averaged solids concentration from both the CFD simulation and the ECT measurements can be compared, and these are shown in Figure 8.

Table 4. CPU Time Demand for 0.1 s Simulation of Drying

Mesh	1	2	3	4	5	6	7
CPU time (s)	0.5	60	187	310	480	600	841

The CFD simulation gives the average solids concentration at three different position values above the air distributor, namely $z = 10$ cm, 15 cm and 20 cm, respectively, while ECT gives the average value at the position $z = 10$ cm above the air distributor. The results from CFD agree well with the ECT measurement with different superficial air velocities. The discrepancy in the center of the vessel is bigger than that in other areas, because of the low-sensitivity of ECT and very low-solids concentration in the center.[37,38]

It can be seen from Figures 6 and 8 that the solids concentration profiles change form U shape to the so-called "crown-like" shape. The main reason can be explained by the bubble mechanism as shown in Figures 3 and 5. At the bottom, due to the small cross-sectional flow area, most of the central area is occupied by air-bubbles, which leads very low-solids concentration in this area, and high-value near the wall region. In the upper region, however, with the increase in cross-sectional area, the bubble behavior changes. A large bubble begins to break up into small bubbles, and some of the solids move upward with the bubble phases in the central area. At the same time, some particles move downward in the near wall region, which results in different solids distribution profile.

Heat and mass-transfer coefficient prediction from CFD simulation

Figure 9 shows the instantaneous parameter distributions obtained by CFD simulation. The superficial air velocity is 2.0 m.s^{-1}, and the particle diameter is 380 μm. From Figure 9a, the solids near the wall move downward, and in the center upward. This movement is reduced by the air-bubble movement in the center of the fluidized bed. The characteristics of the air bubbles, which rise and grow within the bed, exert a profound influence on the fluid dynamics and chemical kinetics.[39] The hydrodynamics play an importance role in the heat and mass transfer in the fluidized-bed dryer, and benefit the mixing of air and solids in the fluidized-bed dryer. Most of the heat and mass flux is transferred in the interarea around the bubble, which can be seen in Figure 9c, d, and e. The same distribution is obtained for the solids temperature as shown in Figure 9f for $t = 10$ s. At $t = 250$ s, the temperature in the bed is nearly the same. The difference between the maximum and minimum values in the bed is only 1.8 K, as seen in Figure 9f for $t = 250$ s.

The characteristics of bubble swarms have not been thoroughly explored and are generally determined from empirical relations for similar beds, leaving major discrepancies unresolved. A number of studies have been reported on the bubble characteristics,[16,40,41] and in this research, the semiempirical model for the bubble frequency is used[42]

$$f_b = \frac{A_b(U - U_{mf})}{\pi/6D_b^3} \tag{22}$$

where D_b is the average diameter of bubbles in the bed, U is the inlet air velocity, and U_{mf} is the minimum fluidization velocity, with both velocities being determined by empirical correlation.[16]

Figure 10 shows the fluctuation in the averaged solids concentration in the bed between the position of z = 5 cm, and z = 20 cm, and the power spectrum obtained by CFD simulation. The dominant frequency from the simulation results,

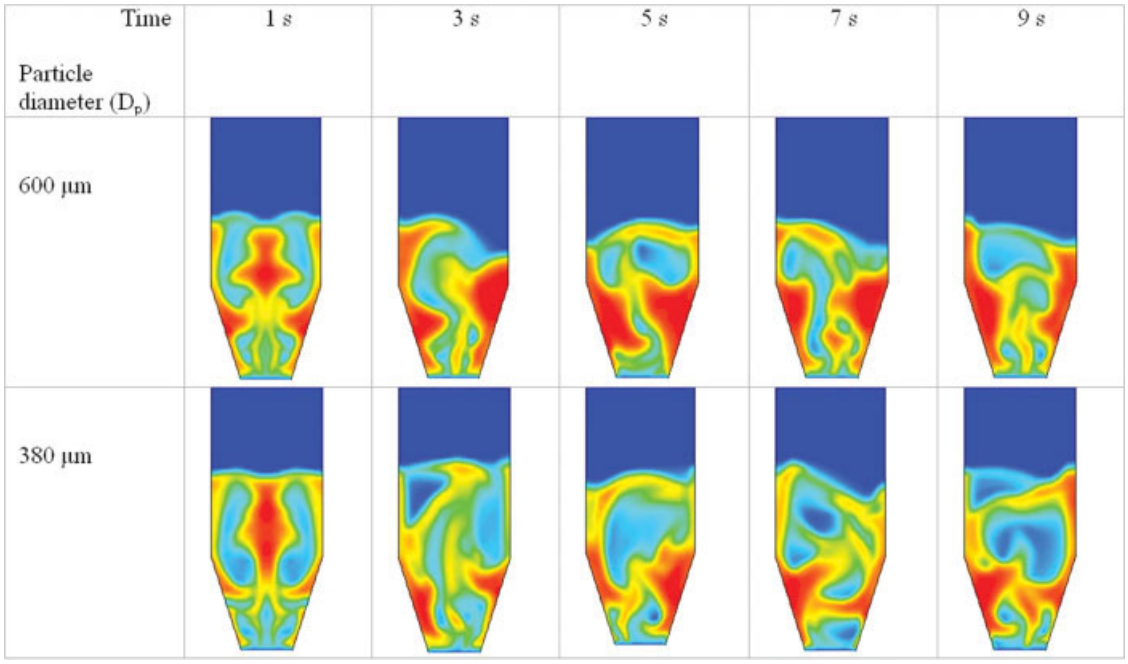

Figure 5. Instantaneous particle concentration distributions obtained by CFD simulation.

[Color figure can be viewed in the online issue, which is available at www.interscience.wiley.com.]

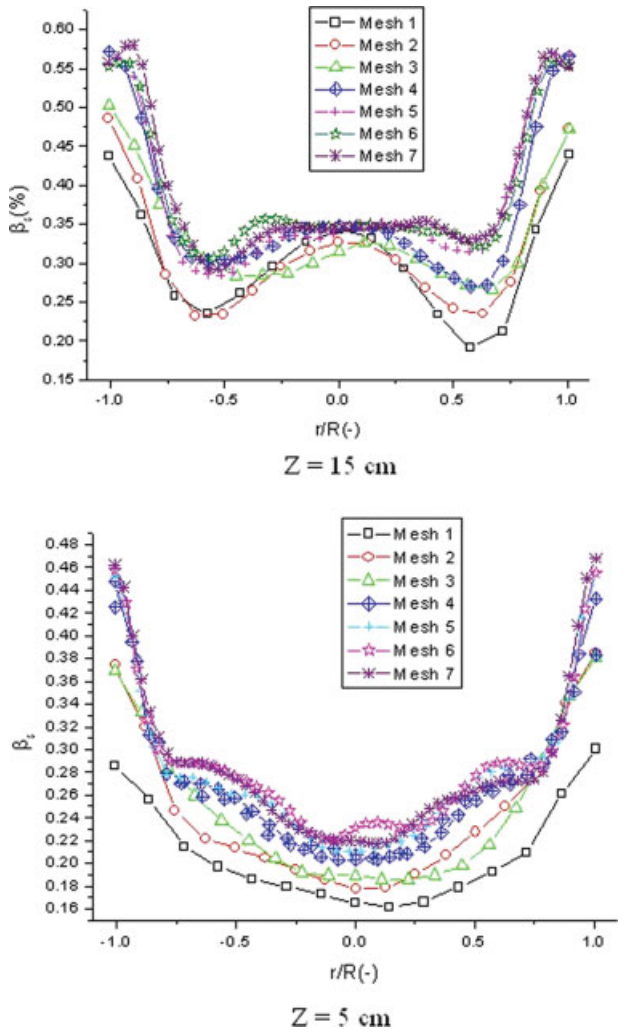

Figure 6. Effect of grid size on the averaged solid concentration.

[Color figure can be viewed in the online issue, which is available at www.interscience.wiley.com.]

and analyzed by the fast Fourier transform (FFT) is 1.8–2.0 Hz. The bubble frequency from the semiempirical Eq. 22 is 3.6 Hz, which is higher than the CFD results. The main reason is that the empirical equation includes the external disturbances, such as the external disturbance to the fluidization air, and the disturbance to an air plenum. Another reason is that the grid size affects the power spectrum distribution. To verify this effect, Figure 11 shows the results at the plane of z = 15 cm with different grid size. It can be seen that the coarse mesh gives poorly predicted results than the fine mesh. For the fine sets of mesh of 2,520 and 6,292, there are still some differences in its spectrum. It means the numerical resolution can be achieved by further increase in the number of grids. However, this is limited by the computer capacity as discussed in the first section. Figure 12 shows the effect of numerical scheme on the resolution of numerical simulation. From these results, it can be seen that the first- and second-order schemes nearly give the same results. For simple geometry and low-speed flow, the first-order scheme can generally be used, instead of the second-order scheme without a significant loss of accuracy. Therefore, all the simulations are based on the first-order unwinding scheme in this research.

The frequent breakup of air bubbles results in fluctuations in the heat and mass transfer within the fluidized bed, as shown in Figure 13 for a range of fluidization velocities. The CFD simulation shows that the heat-and mass-transfer coefficient increase with the increasing fluidization velocity, although the rate of increase reduces when the velocity exceeds 2.0 $m \cdot s^{-1}$. The fluctuation of the heat and mass-transfer coefficients can be seen clearly from the simulation results, which suggests that the air-bubble dynamics play an importance role in heat and mass transfer in fluidized-bed drying, and is the primary reason why the mathematical model is based on bubble hydrodynamics.

Figure 14 a and b shows the time-averaged heat-and mass-transfer coefficient at different positions above the air distributor when the superficial air velocity is $U_0 = 2.0\ m \cdot s^{-1}$, and the particle diameter is 380 μm. The largest values of

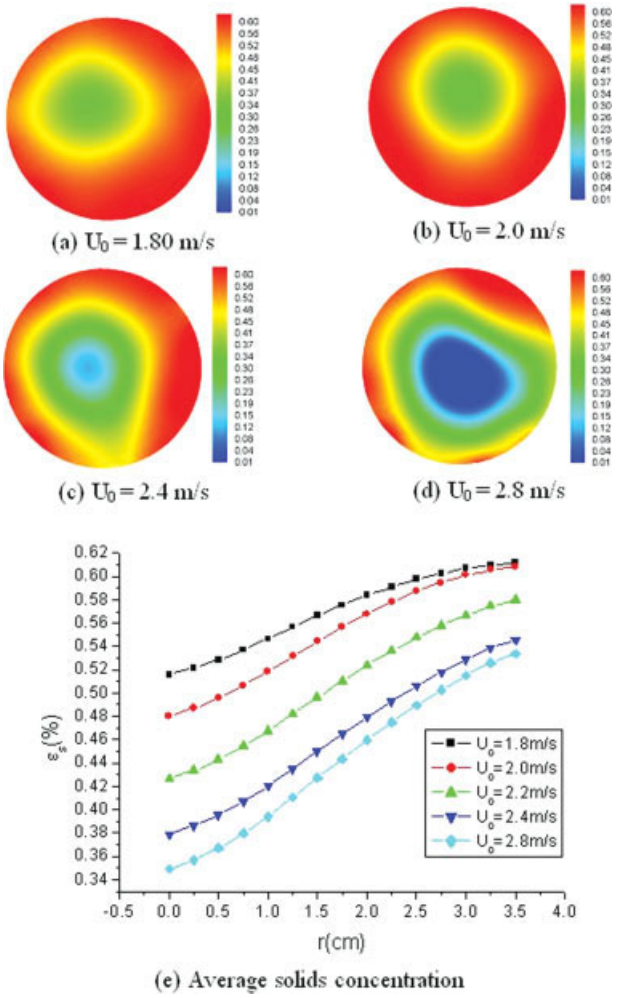

Figure 7. Image reconstruction by ECT with different velocity and average solids concentration.

[Color figure can be viewed in the online issue, which is available at www.interscience.wiley.com.]

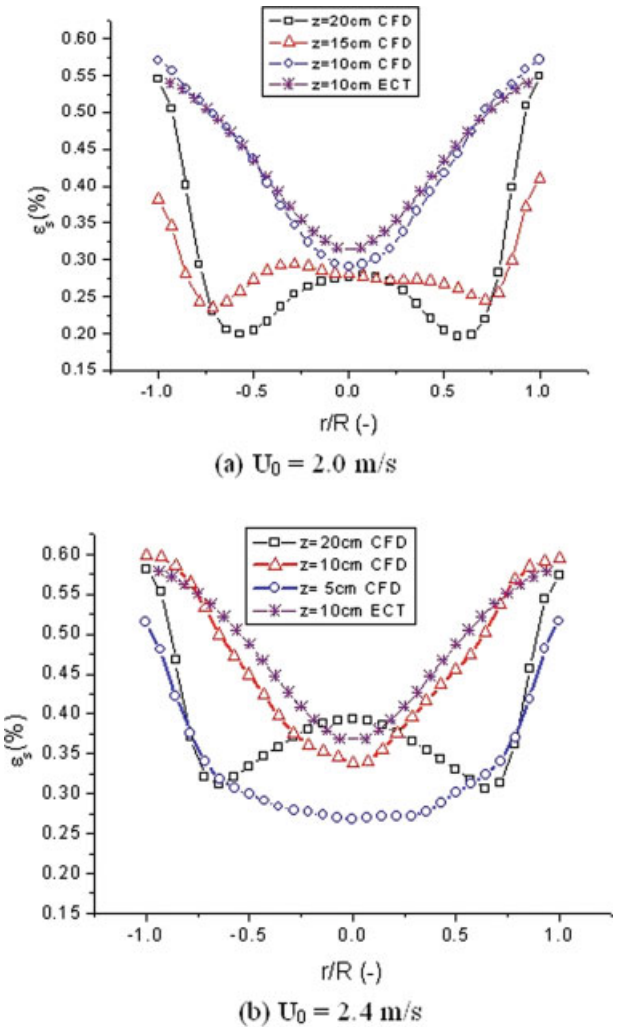

Figure 8. Average solids concentration at different position above air distributor.

[Color figure can be viewed in the online issue, which is available at www.interscience.wiley.com.]

heat and mass transfer occur at positions $z = 15$ cm above the air distributor. In the range $z = 0$ cm to 15 cm, the local average heat-and mass-transfer coefficients increases with the increasing bubble height. Above this range, these parameters decrease sharply. The changes in these trends can be attributed to both of the particles Re_p and Sch number as depicted in Figure 14c. After the position of $z = 12$ cm, the Sch number sharply decrease. This is an important parameter in calculation of mass-transfer coefficient as given in Eqs. 15 and 16. This distribution profiles lead to the decrease in mass-transfer coefficient after this position. The same trends and mechanism are also applied to the heat-transfer coefficient.

Measurement of moisture and temperature

A fluidized-bed drying process has three distinct periods: prewarming; constant-rate drying and falling-rate drying.[2] Figure 15 shows the changes in moisture and temperature, obtained using a moisture meter and a thermocouple, respectively, during a batch fluidized-bed drying process, together with the predictions from the mathematical modeling, shown by solid lines. The initial moisture content was set to be 23%, and dried to 1.5% at the endpoint. The three distinct periods can be clearly seen from the temperature curve, and the mathematical model agrees well with the measurement results. Figure 15 also shows the measurement errors compared with mathematical modeling for 15 batch drying processes. The error bar shown in this curves is 5%.

There are two main reasons for the disagreement between the measurement and mathematical modeling. One is that the three-phase theory for bubbling fluidized bed is derived from the fluidized bed with a cylindrical vessel, but the measurement in this research is based on the conical vessel. The nature of bubble migration does depend on geometrical effects,[39] so the hydrodynamic characteristics of bubble will be different in these two types of fluidized beds. The effect of geometry on the drying process with conical chamber is a topic of current research. Another reason for the discrepancy is that the treatment of the fluidized bed wall is different. In the mathematical modeling, the wall is treated as an insulator with no heat flow across the boundary, but in practice, heat is lost to the surroundings through the walls. This can be corrected by changing the wall boundary conditions in mathematical modeling.

Figure 16a shows a drying curve, from which the drying rate that is, the gradient of X_p, can be derived by applying a difference operator to the drying times. Figure 16b shows the drying rate based on the measurement results as shown in Figure 16a. From the drying rate, it is difficult to obtain the prewarming drying rate, because the heating during this phase of the process is rapid, so only a few measurement points can be obtained. The constant and falling-rate periods are clearly shown in Figure 16. Most of the test measurement errors fall in the range of 10% compared with the mathematical modeling.

The operating parameters, in particular the superficial air velocity and humidity of the drying medium, have a marked effect on the drying processes.[10] The influence of the superficial air velocity and inlet air humidity on the performance characteristics of the fluidized-bed dryer as predicted by CFD simulation, can be seen in Figure 17. When the superficial gas velocity U_0 increases, the average temperature of particles increases, while the average moisture content reduces sharply, which is due to the increased mass-and heat-transfer between bubbles, emulsion air and solids. With the increase of inlet air humidity, the temperature during the constant-rate period is increased by about 3°C, because the drying balance temperature, that is, the wet bulb temperature depends on the inlet air humidity: the higher the inlet air humidity, the more latent heat evaporates the water from the surface of the particles. These results agree with the mathematical modeling results.[15] Hence, the inlet air humidity should be reduced during drying process. Because CFD simulation is very time-consuming, only 5 min have been simulated for the prewarming and constant-rate drying periods. From Figure 17a, it can be concluded that with the increase in fluidization velocity, the drying rate is increased. This agrees with the mathematical results.[10,15]

From the previous analysis, it can be seen that CFD simulation can provide details of the heat and mass transfer in the

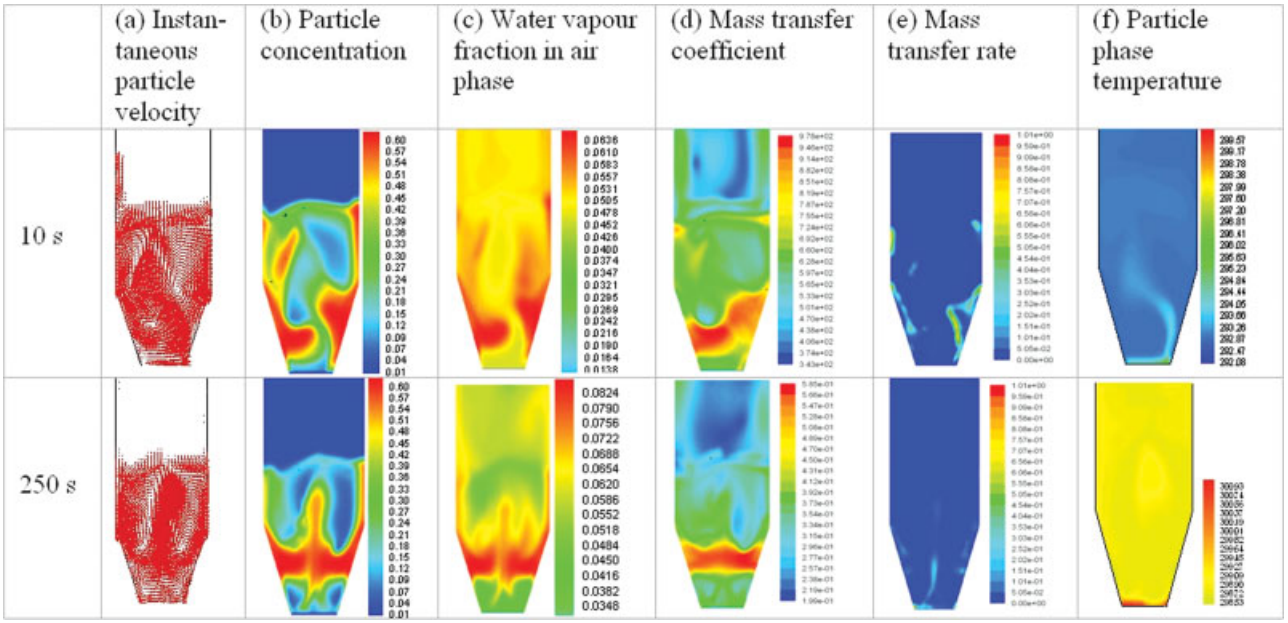

Figure 9. Instantaneous parameter distribution from CFD simulation.

[Color figure can be viewed in the online issue, which is available at www.interscience.wiley.com.]

fluidized-bed dryer, and predict the effect of operational parameters, that is, the superficial air velocity and the inlet air humidity, on the drying process. This indicates that this two-fluid model can be applied to the fluidized-bed dryer for design and optimization. The ECT measurement results indicate that ECT cannot only provide the instantaneous parameter distribution in a cross section, but also an accurate

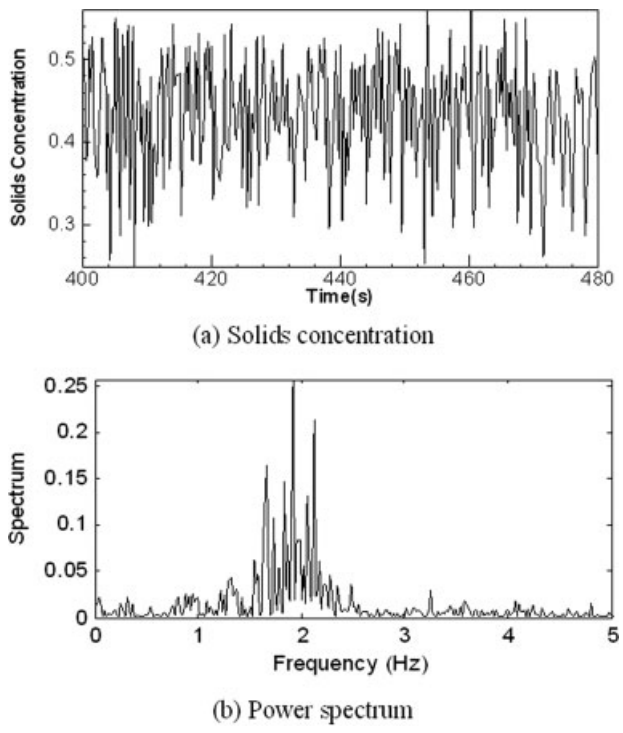

Figure 10. Fluctuations obtained by CFD simulation.

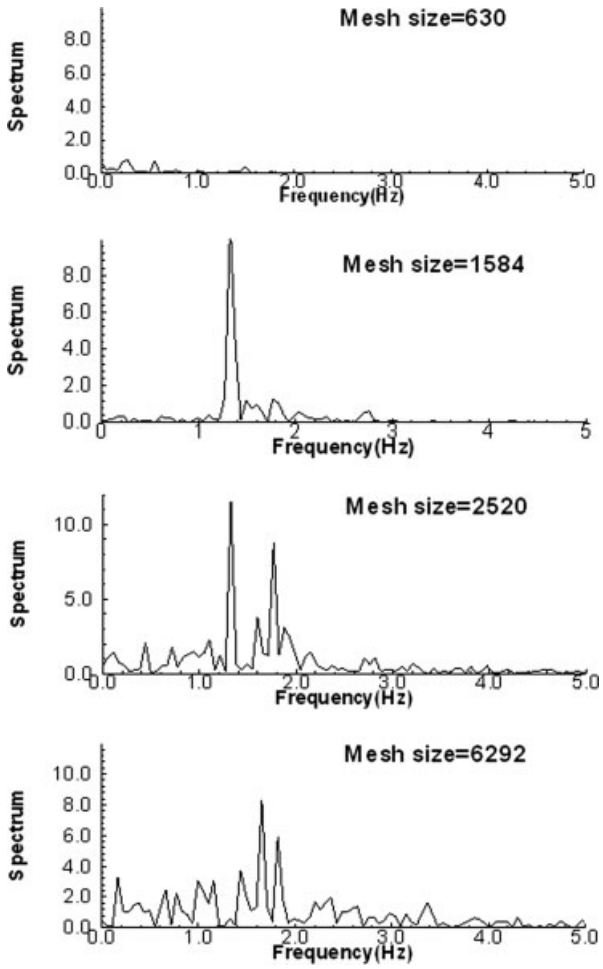

Figure 11. Power spectrum obtained by different grid size for single points in the bed.

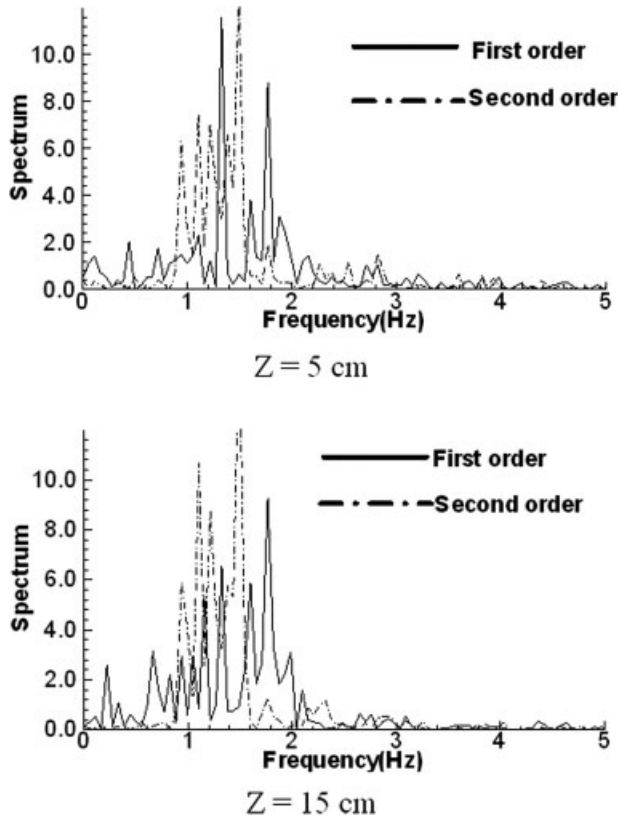

Figure 12. Power spectrum obtained by first- and second-order numerical scheme for single points in the bed.

time-average, in good agreement with the CFD simulation. Compared to the reference measurements, the mathematical model is sufficiently accurate for process modeling of the entire drying process.

Due to the bubble size and velocity in fluidized bed varies widely from system to system,[16] the mathematical model based on the three-phase theory should be adjusted to different fluidized-bed system, especially for different geometry and shape of fluidized beds. From the aforementioned CFD simulation, it can be seen that CFD can give the detailed parameters distribution during the drying process with different initial conditions and operational parameters. This can reduce the experimental test period and save operating cost. Form this point of view, CFD simulation is useful for process design and optimization.

Dynamic measurement of moisture content

To obtain a reference for moisture content, a sample of approximately 2.5 g was taken from the fluidized bed every 5 min during a drying process, and then measured using the moisture meter. The meter is accurate but slow, because it is based on weight loss and takes several minutes for measuring a sample. In this research, a alternative approach based on static and dynamic calibration of the ECT measurements has been developed. The capacitance is a function of the material permittivity and its geometric configuration

$$C_M = \sigma_0 \sigma_{eff} \Phi \tag{23}$$

where σ_0 is the electric constant, σ_{eff} is relative permittivity, and Φ is geometric constant. Typically, the capacitance is a function of the area of electrodes and the distance between them. The relative permittivity of the material in the fluidized-bed dryer can be expressed as a function of solids concentration and moisture content

$$\sigma_{eff} = \phi(\varepsilon_s, X_p) \tag{24}$$

The normalized capacitance is defined as

$$C_N = \frac{C_M - C_L}{C_H - C_L} \tag{25}$$

For the dry material, the permittivity and capacitance are affected only by the solids concentration. From ECT, the solids concentration can be estimated, and the effective permittivity

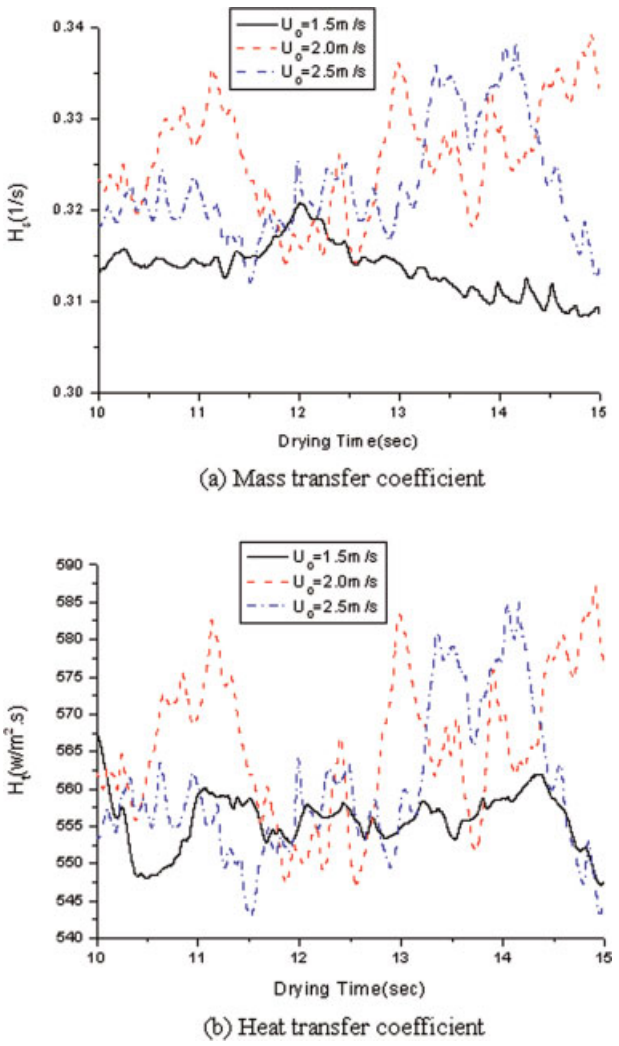

Figure 13. Average mass- and heat-transfer coefficient with different superficial gas velocity.

[Color figure can be viewed in the online issue, which is available at www.interscience.wiley.com.]

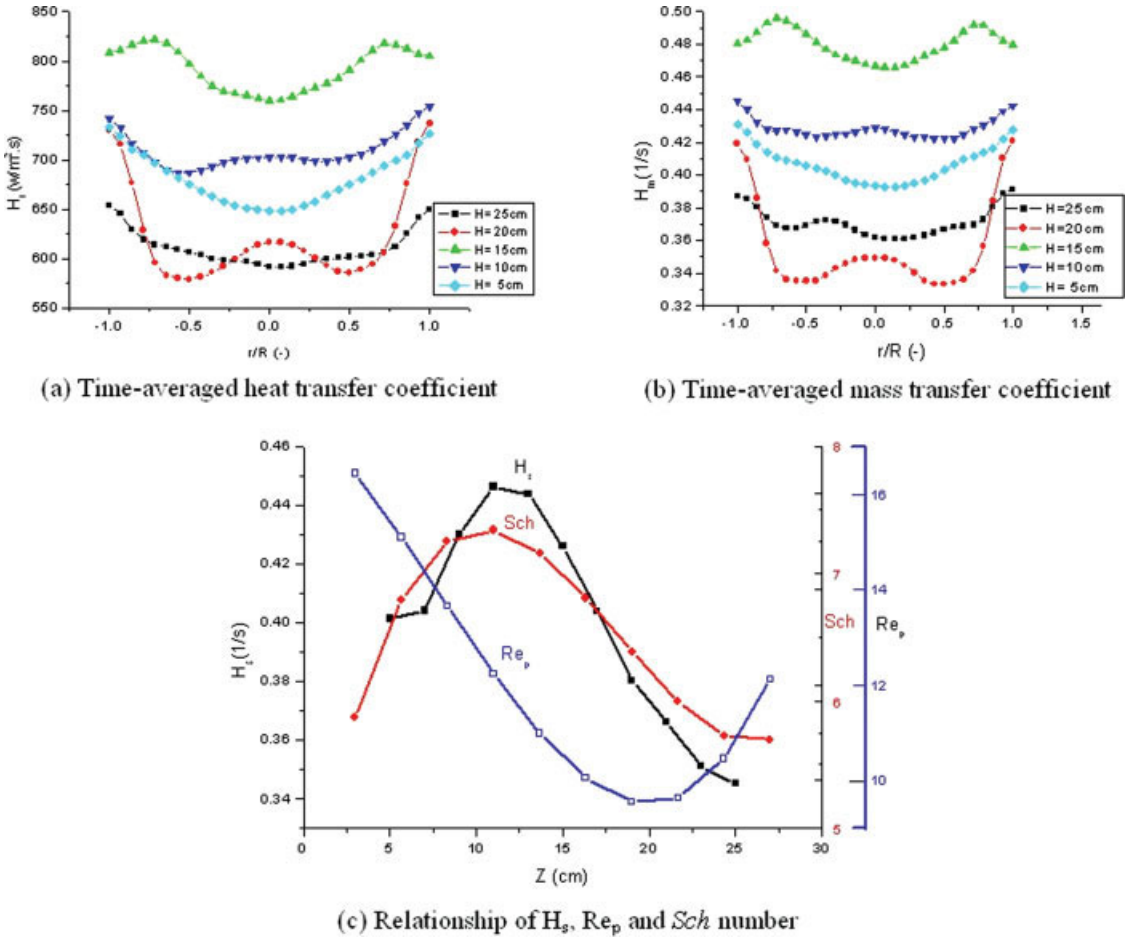

Figure 14. Average mass and heat-transfer coefficient at different position above the air distributor.

[Color figure can be viewed in the online issue, which is available at www.interscience.wiley.com.]

of the mixing can be derived using different permittivity models. In our research, this normalization is not valid due to the change in moisture content throughout the drying process. The high-permittivity calibration value in Eq. 25 changes with the drying times. Therefore, a dynamic calibration based on the change in moisture is needed.

For the 12-electrode ECT sensor used in this research, there are a total of 66 capacitance measurements, each having its own sensitivity area, namely sensitivity map,[43] which means the changes in capacitance due to the different permittivity distribution between two measurement electrodes. For an adjacent electrode pair, the sensitivity area is localized to a small region. Figure 18 shows the capacitance between adjacent electrode pairs, and the capacitance between opposite electrode pairs. It can be seen that the capacitance of adjacent electrode pairs nearly keeps constant with the increase of U_0. The adjacent pairs capacitance only affected by is neighbor area, namely sensitivity area. However, the opposite pairs capacitance rapid decrease with the increase in superficial air velocity. Because the superficial air velocity is strictly controlled in the range of 0.2–2.2 $m.s^{-1}$, the capacitance of adjacent electrode pairs is only affected by the operator condition (i.e., superficial air velocity), and the moisture content during the drying process. At a constant superficial air velocity, the capacitance of adjacent electrode pair is only affected by solids concentration in the local region.

For a bubbling bed, the solids concentration presents a special distribution, the so called "crown-like shape".[44] In this type of distribution, the solids concentration in the central area is low and the solids concentration near the wall is high as shown by the results from the CFD simulation in Figure 7, and the ECT measurements in Figure 6. The solids concentration in the near wall region is nearly the same as that at the minimum fluidizing conditions, while the cross-sectional area is largely occupied by solids scattered with air bubbles. Combining the characteristics of solids concentration with a sensitivity map, the capacitance measured from the adjacent electrode pairs is useful for dynamic calibration. The moisture measurement is based on dynamical calibration as described in the following.

First, a set of static calibration data is taken using the ECT sensor with different moisture content at the packed-bed conditions when there is no fluidizing gas flow. A second set of calibration data is then taken at the minimum fluidization conditions. During the drying process, a third set of measured capacitance is taken without shutting down the fluidized bed, for dynamic calibration. The two sets of static calibration data are combined with the dynamic calibration

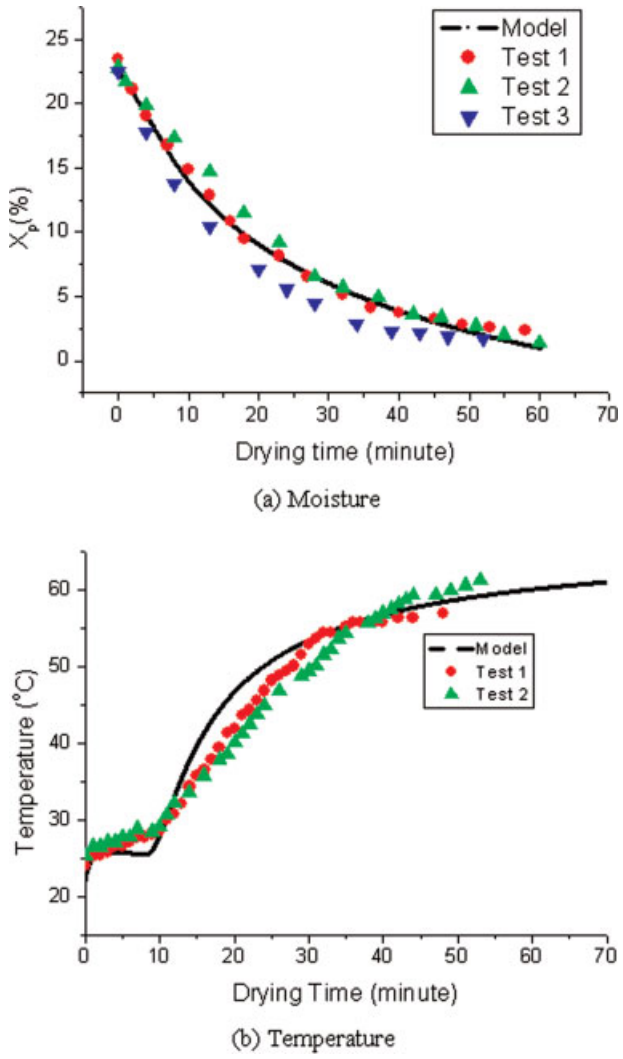

Figure 15. Moisture and temperature curves of batch fluidized-bed drying.

[Color figure can be viewed in the online issue, which is available at www.interscience.wiley.com.]

data to determine the online moisture content. Due to air bubbles passing through the measurement area during the drying process, only the capacitance between the adjacent electrode pairs is used for dynamic calibration as the other capacitance measurements have little relationship with the static calibration data. The static calibration process is actually the same as normal calibration, that is, obtaining C_L with air as a low-permittivity material, and obtaining C_H with wet granule as a high-permittivity material. The difference between the dynamic and static calibration is that the first only needs high-permittivity data, keeping C_L fixed, but C_H being changed with moisture. It was found that the data could be represented by a third-order polynomial fit to the two sets of static calibration data.

$$C_p(X_p) = \sum_{n=0}^{n=3} a_i X_p^n \tag{26}$$

where a_i is the regression coefficient, and n is the order number.

As there are 66 independent capacitance measurements, 66 polynomial fit curves are needed with different coefficient of a_i. From these calibration curves, the moisture can be determined by interpolation of the dynamic data using the calibration fit curves, which is similar to the method used by Chaplin.[46] The high calibration data, namely 66 capacitance values of C_H in Eq. 25, can be determined from the data at the packed-bed conditions, and used for online image reconstruction. The dynamic calibration is different from that provided by Chaplin in that it does not need to shut shown the air supply during the entire drying process.

Because there are 11 independent adjacent electrode pairs, there are 11 interpolation errors when the dynamic calibration data are used, so 11 different moisture contents can be obtained at the same time, and the average value is used to determine the moisture content. Figure 19 shows a measurement result for adjacent electrode pair in the minimum fluidization conditions and dynamic calibration during the drying process. Figure 20 shows three tests for static and dynamic

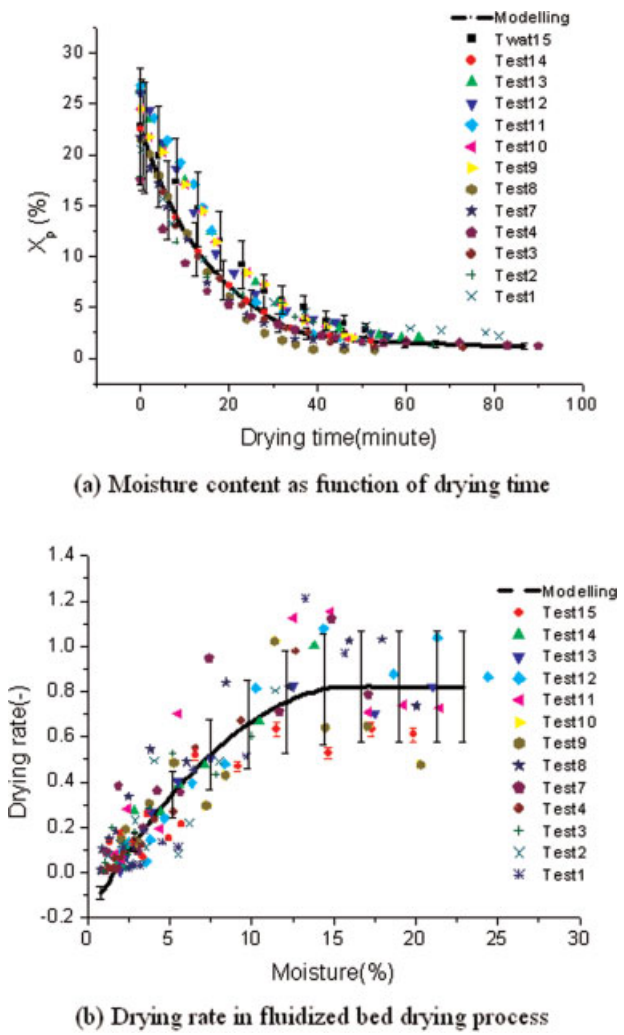

Figure 16. Moisture content and drying rate.

[Color figure can be viewed in the online issue, which is available at www.interscience.wiley.com.]

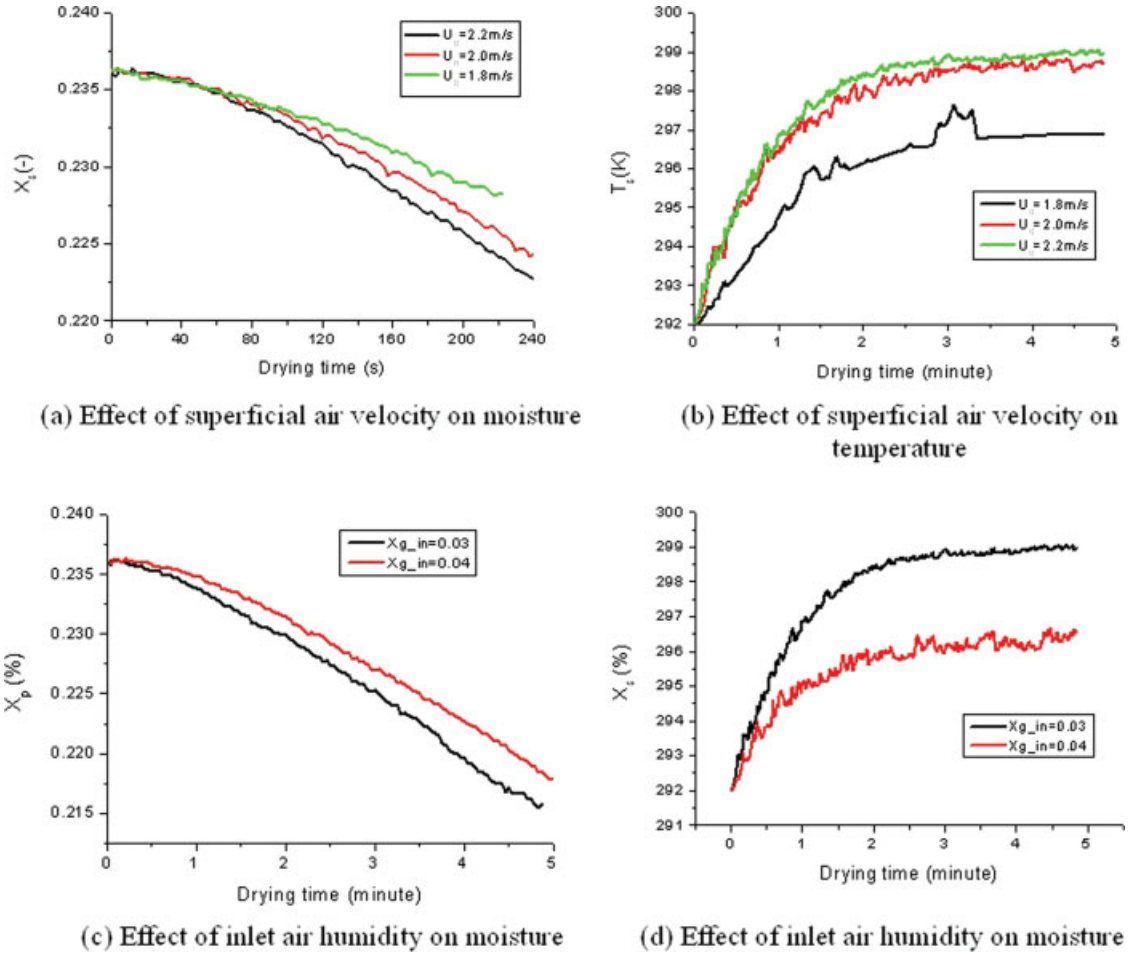

Figure 17. Moisture and temperature predicated by CFD.

[Color figure can be viewed in the online issue, which is available at www.interscience.wiley.com.]

calibration, indicating that the static capacitance is slightly larger than the dynamic capacitance for adjacent electrode pairs due to the minimum air fraction. The measurement result shows a good relationship between the static and dynamic capacitance. To verify the ECT measurement method, Figure 21 gives the ECT measurement results, which are compared with the reference method. From the calibration curves, it can be seen that most of the ECT measurement results fall within 5% errors compared with the results measured by the moisture meter.

Figure 22 shows the change in moisture content during the entire fluidized-bed drying, by ECT based on the aforementioned measurement method, mathematical modeling and reference. Although the static measurement is more accurate, the dynamic measurement provides sufficient information for determining the endpoint of the fluidized-bed drying process. The advantage of the dynamic measurement is that it does not need to shut down the air supply, and, hence, can improve the operating efficiency.

The standard deviation (SD) is used to compare the different measurement methods and the calculated results are given in Table 5. Compared to the reference and the static calibration method,[45] the dynamic measurement is slightly more accurate than the previous methods when the moisture content is >5%. Outside this range, the two methods are nearly the same, especially close to the endpoint of drying. In terms of SD, the static method is nearly the same as the reference. The dynamic value of SD is slightly larger than the other methods.

Permittivity and density distribution

In Eq. 25, a parallel model is assumed. Together with a series model and the Maxwell model, they can be expressed as

$$\phi(\varepsilon_s, X_p) = (1-\varepsilon_s).\sigma_g + \varepsilon_s \cdot \sigma_s(X_p) \tag{27}$$

$$\phi(\varepsilon_s, X_p) = \frac{1-\varepsilon_s}{\sigma_g} + \frac{\varepsilon_s}{\sigma_s(X_p)} \tag{28}$$

$$\phi(\varepsilon_s, X_p) = \frac{3\sigma_g - 2(1-\varepsilon_s)(\sigma_s(X_p) - \sigma_g)}{3\sigma_g + (1-\varepsilon_s)(\sigma_s(X_p) - \sigma_g)} \tag{29}$$

From these models and a known solids concentration, the effective permittivity of the fluidized materials can be found. In a fluidized-bed dryer, there are three components: dry solids; water in solid phase and air, so these permittivity models cannot be applied directly. However, the permittivity models can be used for the solids phase because it contains two

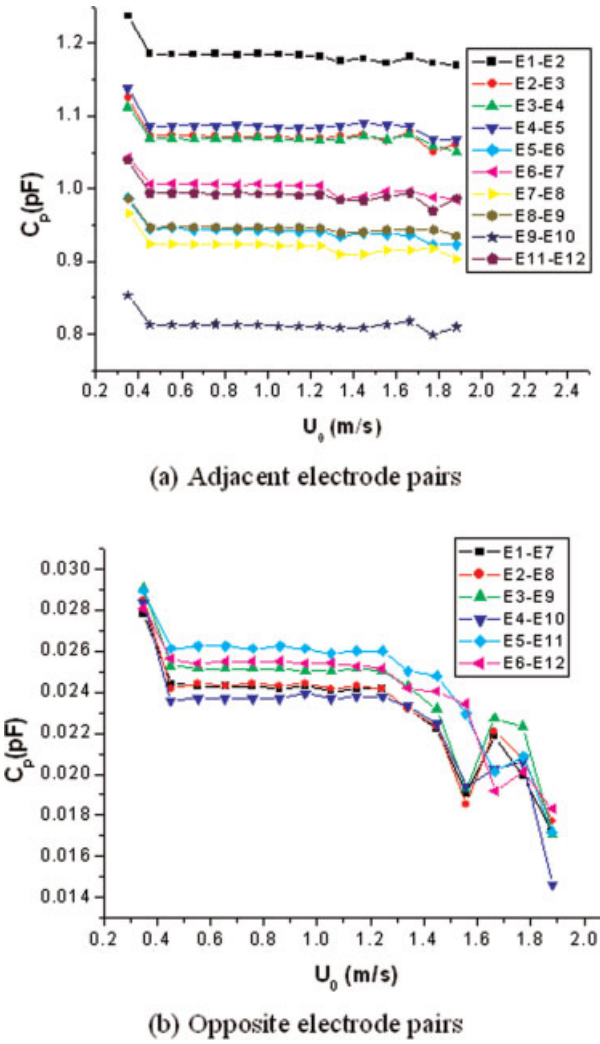

Figure 18. Capacitance as function of superficial gas velocity.

[Color figure can be viewed in the online issue, which is available at www.interscience.wiley.com.]

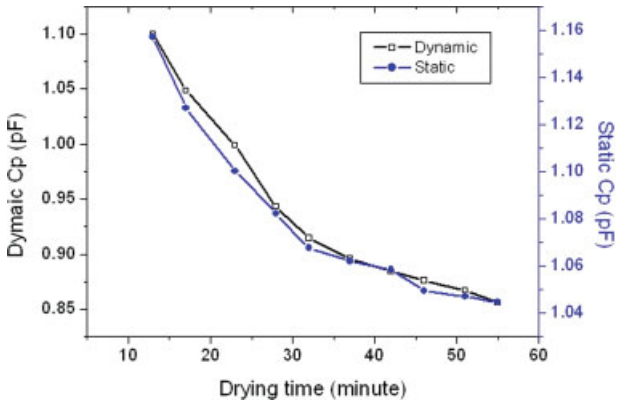

Figure 19. Dynamic and static calibration capacitance for adjacent electrode pair.

[Color figure can be viewed in the online issue, which is available at www.interscience.wiley.com.]

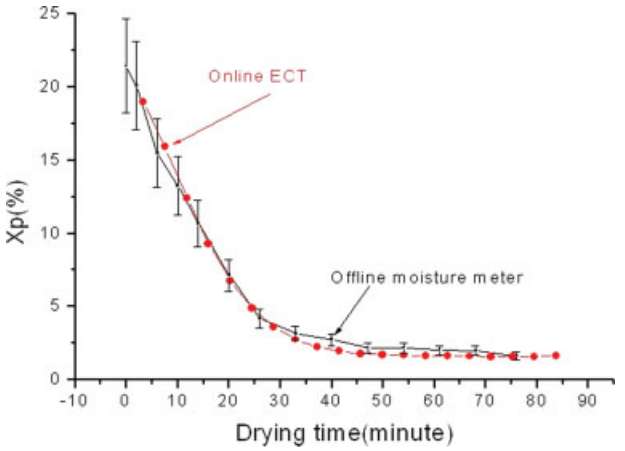

Figure 20. Moisture measurement by ECT vs. reference measurement method.

[Color figure can be viewed in the online issue, which is available at www.interscience.wiley.com.]

components. Equations 27–29 can be used to obtain three different permittivity values σ_s. With a known σ_s and solids-volume fraction ε_s, the effective permittivity can be derived. Based on this combined method, there are nine different results. It has been found that only the Maxwell model can give good results for the solids permittivity. Therefore, three combined models, Maxwell-Series, Maxwell-Parallel and Maxwell-Maxwell, are used. These combined models are similar to the three-phase model used in gas-solid-liquid fluidized bed.[46]

According to the model for a parallel-plate capacitor and Eq. 23, the relative permittivity can be obtained from the high-and low-capacitance data by ECT. Figure 18 shows the ECT measurements compared with the above three permittivity models. Figure 23a shows the results with initial moisture of 18% and Figure 23b with 24%. In the both cases, the Maxwell-Series model presents the best result to give the

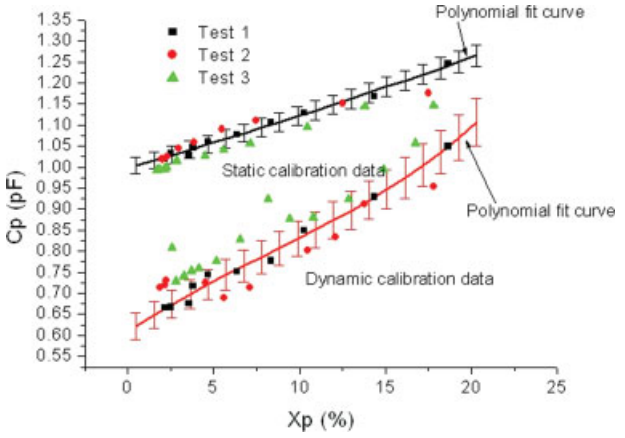

Figure 21. Capacitance of adjacent electrode pairs with different moisture content.

[Color figure can be viewed in the online issue, which is available at www.interscience.wiley.com.]

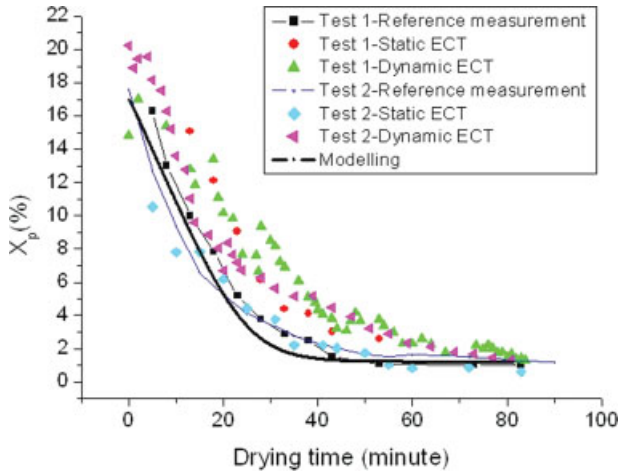

Figure 22. Moisture content measured by ECT and mathematical modeling, compared with reference.

[Color figure can be viewed in the online issue, which is available at www.interscience.wiley.com.]

permittivity distribution when the moisture content is <18%. Out of that range, all three models fail to give accurate results, when compared to the ECT measurement.

Based on the moisture content and the solids density Eq. 20, the cross-sectional distribution can be obtained as shown in Figure 24 for different levels of moisture content. The local regions of the adjacent electrode pairs are not always occupied by solids, as shown in Figure 6, for the case where $U_0 = 2.8\ \mathrm{m \cdot s^{-1}}$, where there is an air bubble close to an adjacent pair. In this case, the dynamic calibration, based on the polynomial fit curves, will give incorrect results, although this situation may be avoided by online imaging tracing. For dynamic calibration, the original data C_M, and the initial calibration data C_L and C_H, are used to reconstruct an image. While the position of bubble is correct in the image, the solids concentration is different because of the unknown high-calibration capacitance C_H in Eq. 23. This continues until the bubble lies in the central region of the measurement zone. A time-averaged estimate of the capacitance taken over about 100 frames, could be used to reduce the measurement error.

Conclusions and Discussion

Numerical study using a mathematical mode, the two-fluid model and ECT has been carried out to investigate the performance and characteristics of a fluidized-bed dryer. The two-fluid model can describe the drying process accurately. The effect of grid size on numerical resolution has been analyzed. The influence of parameters and mechanisms on the drying process has been discussed theoretically and investigated experimentally.

The experimental setup is suitable for validation of the mathematical model, and numerical simulation and the experimental data obtained are in good agreement with the numerical results. This indicates that the developed two-fluid model is suitable as the basis of simulations, because the hydrodynamics of the fluidized-bed dryer incorporated both mass-and energy-transfer. A dynamic calibration procedure has been implemented for ECT measurements, which is based on a polynomial fit of the static calibration for the packed bed, and the minimum fluidization bed capacitance taken through the drying process. This has been validated by a reference method. The permittivity analysis result indicates that the Maxwell-Series model accurately estimates the effective permittivity in the fluidized-bed drying process. The online moisture measurement, based on both dynamic and static calibration can determine the endpoint of drying, and a comprehensive validation indicates that dynamic calibration

Table 5. Standard Deviation (SD) of Measurement Results

Test	Reference Measurement	Static Measurement by ECT	Dynamic Measurement by ECT
1	4.23	4.18	4.73
2	4.74	4.65	6.19

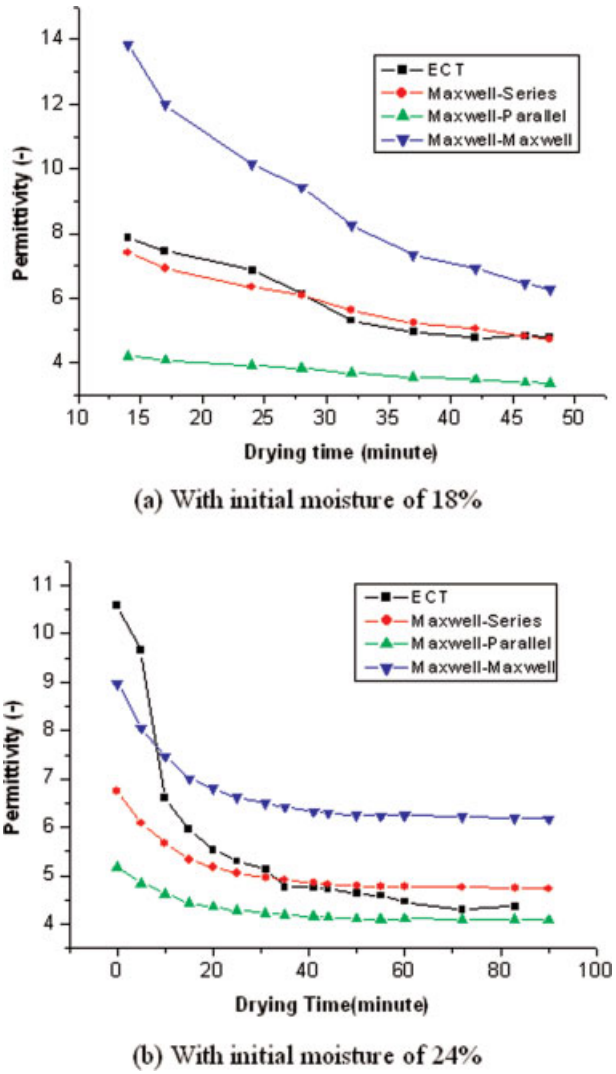

Figure 23. Moisture distribution with drying time.

[Color figure can be viewed in the online issue, which is available at www.interscience.wiley.com.]

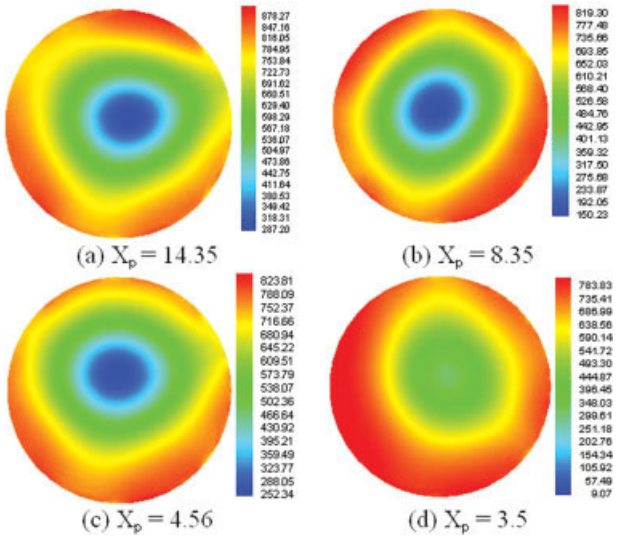

Figure 24. Solids-density distribution with different moisture content.

[Color figure can be viewed in the online issue, which is available at www.interscience.wiley.com.]

for ECT combined with the mathematical modeling is a powerful tool for online moisture measurement and process modeling.

The online moisture measurement assumes that the effect of temperature on the ECT sensor wall can be neglected. However, during the drying process, the temperature of solids phase changes from 20°C to 60°C at the endpoint of drying. Also, the temperature of the sensor wall changes from the temperature at ambient conation to 40–50°C, depending on the temperature of solids phase at the endpoint of drying. Because the relative permittivity of water and wall material is a function of temperature,[47] the effect of wall temperature on measurement should be measured and controlled online. The hydrodynamic effect, such as the restitution coefficient due to the change in moisture content during the drying process, has not been considered in the mathematical model and CFD simulation, and is a current topic of research. Further research on the role of CFD simulation in online mathematical modeling will also be addressed.

Acknowledgments

The authors would like to thank EPSRC (GR/T29383/01, GR/T29376/01) for sponsoring the research. Mike Claybourn and Steve Foster of AstraZeneca, David Scott of DuPont and Tom Bach of Sensatech are thanked for collaboration.

Notation

A = cross-sectional area of bed, m^2
$A_{p,s}$ = particle surface area, m^2
Bi = biot number
C_d = drag coefficient
c_g = thermal capacity of air phase, $J \cdot kg^{-1} \cdot K^{-1}$
c_p = thermal capacity of particle, $J \cdot kg^{-1} \cdot K^{-1}$
c_s = thermal capacity of solids phase, $J \cdot kg^{-1}\ K^{-1}$
C = measured capacitance, pF
d_p = mean particle diameter, m
D_b = bubble diameter, cm
D_v = vapor diffusion coefficient in air, $m^2 \cdot s^{-1}$
$D_{v,s}$ = water diffusion coefficient in solids, $m^2 \cdot s^{-1}$
F = bubbling frequency, Hz
g = acceleration due to gravity, $m \cdot s^{-2}$
H = height of bed, cm
h = entropy, KJ
h_s = mass-transfer coefficient, $kg\ m^{-2}\ s^{-1}$
h_t = heat-transfer coefficient, $J/m^2 \cdot s$
$\dot{m}$ = convective mass transfer, $kg \cdot m^{-1}\ s^{-1}$
N_p = number of particle reflecting density
Nu = nusselt number
p = pressure, pa
P_{sat} = saturated pressure, pa
Pr = prandtl number
$\dot{q}$ = convective heat transfer, $W \cdot m^{-1}\ s^{-1}$
r = radial direction, m
Re = Reynolds number
Sc = Schmidt number
Sch = Sherwood number
T = temperature, K
U_0 = superficial air velocity, $m \cdot s^{-1}$
V = velocity, $m \cdot s^{-1}$
X_s = equilibrium moisture content, $kg \cdot kg^{-1}$
X_s^* = equilibrium moisture in particles, $kg \cdot kg^{-1}$
Y = vapor fraction in air phase

Greek letters

β = drag coefficient
ε = volume fraction
θ = kinetic temperature
λ = thermal conductivity, $W.m^{-1}.K^{-1}$
ρ = density, $kg.m^{-3}$
σ = permittivity
μ = viscosity, $kg.m^{-1}.s^{-1}$
Φ = geometry factor

Subscripts

g = air phase
l = liquid
M = measurement
N = normalize
p = particle
s = solids phase
W = water

Literature Cited

1. Davidson JF, Clift R, Harrison D. *Fluidization*. Academic Press: London, UK 1985.
2. Vojtěch VC Sc, Markvart M, Drbohlav R. *Fluidized bed drying*. Leonard Hill: London, UK; 1966.
3. Roman GS, Andrzej K. Point-by-point solution procedure for the computational fluid dynamics modelling of long-time batch drying. *Ind Eng Chem Res*. 2005;44:7892–7898.
4. Roman GS, Kmiec A. CFD modelling of heat and mass transfer in a Spouted Bed dryer. *Ind Eng Chem Res*. 2004;43:1113–1124.
5. Kemp IC, Oakley DE, Bahu RR. Computational fluid dynamics modelling of vertical pneumatic conveying dryers. *Powder Technol*. 1991;65:477–484.
6. Skuratovsky I, Levy A, Borde I. Two-fluid, two-dimensional model for pneumatic drying. *Drying Technol*. 2003;21:1649–1672.
7. Wang HG, Yang WQ, Dyakowski T, Senior P, Raghavan RS. Investigation of fluidised bed drying by combination of CFD and ECT. Proc. of 4th Int. Symp. on Process Tomography in Poland; 14–15 Sept, 2006; Warsaw, Poland. pp 110–114.
8. Palancz B. A mathematical model for continuous fluidized bed drying. *Chem Eng Sci*. 1983;38:1045–1059.
9. Viswanathan K, Hamdullahpur F. Mathematical modelling of simultaneous heat and mass transfer in fluidized bed drying of large particles. *Canadian J of Chem Eng*. 1986;64:87–95.

10. Lai FS, Chen YM, Fan LT. Modelling and simulation of a continuous fluidized bed dryer. *Chem Eng Sci*. 1986;41:2419–2430.
11. Garnavi L, Kasiri N, Hashemabadi SH. Mathematical modelling of a continuous fluidized bed dryer. *Int Communications in Heat and Mass Transfer*. 2006;33:666–675.
12. Aly SE, Fathalah KA. A three-phase model of a bath fluidized bed. *Heat and Mass Transfer*. 1999;34:405–412.
13. Kannan CS, Rao SS, Varma YBG. Kinetic model for drying of solids in batch fluidized beds. *Ind Eng Chem Res*. 1994;33:363–370.
14. Lee DH, Kim SD. Mathematical model for batch drying in an inert medium fluidized bed. *Chem Eng, Technol*. 1999;22:443–450.
15. Wang HG, Dyakowski T, Senior P, Raghavan RS, Yang WQ. Modelling of batch fluidised bed drying of pharmaceutical granules. *Chem Eng Sci*. 2007;62:1524–1535.
16. Kunii D, Levenspiel O. *Fluidization Engineering*. Boston: Butterworth-Heinemann; 1991.
17. Hosabettu NH, Subramanian N. Three-phase model for gas flow in fluidized beds. *Ind Eng Chem Fundam.* 1982;21:85–87.
18. Rantanen J, Lehtola S, Rämet P, Mannermaa J-P, Yliruusi J. On-line monitoring of moisture content in an instrumented fluidized bed granulator with a multi-channel NIR moisture sensor. *Powder Technol*. 1998;99:163–170.
19. Mattes RA, Root DE, Birkmire AP. In-line process analysis of residual moisture in a fluid bed granulator-dryer using NIR spectroscopy. *The Role of Spectroscopy in Process Analytical Technologies*. 2005; 14–17.
20. King RJ, King KV, Woo K. Microwave moisture measurement of grains. *IEEE Trans on Instrum. and Meas*. 1992;41:111–115.
21. Davies C, Talion S. In-line density-compensated moisture measurement in free-flowing bulk solids with an off-the-shelf capacitance level prove. Proc. of AIChE Annual Meeting; Nov. 7–12, 2004; Austin, Texas. pp 3197–3200.
22. Young L. Moisture measurement using low resolution nuclear magnetic resonance. *Measurement + Control*. 1989;22:54–55.
23. McKenzie P, Kiang S, Tom J, Rubin AE, Futran M. Can pharmaceutical process development become high tech. *AIChE J*. 2006;52:3990–3994.
24. Lun CKK, Savage SB, Jeffrey DJ. Chepurniy N. Kinetic theories for granular flow: Inelastic particles in coquette flow and slightly inelastic particles in a general flow field. *J Fluid Mech*. 1984;140:223–256.
25. Ding J, Gidaspow D. A bubbling fluidization model using kinetic theory of granular flow. *AIChE J*. 1990;36:523–538.
26. Gidaspow D, Bezburuah R, Ding J. Hydrodynamics of circulating fluidized bed, kinetic theory approach. In: Fluidization VII. Proc. of 7th Eng. Foundation Conference on Fluidization; 3–8 May, 1992;75–82; Brisbane, Australia.
27. Gidaspow D, Ettehadieh B. Fluidization in two dimensional beds with a jet: Part II. Hydrodynamic modelling, *Int Eng Chem Fundam.* 1983;22:193–201.
28. Gunn DJ. Transfer of heat or mass to particle in fixed and fluidised beds. *Int J Heat and Mass Transfer*. 1978;21:467–476.
29. Johnson PC, Jackson R. Frictional-collisional constitutive relations for granular materials with application to plane shearing. *J Fluid Mech*. 1987;176:67–93.
30. Sinclair JL, Jackson R. Gas-particle flow in a vertical pipe with particle-particle interactions. *AIChE J*. 1989;35:1473–1486.
31. Yang WQ, York TA. New AC-based capacitance tomography system. *IEE Proc-Sci Meas Technol*. 1999;146:47–53.
32. Liu S, Wang HG, Jiang F, Yang WQ. A new image reconstruction method for tomographic investigation of fluidized beds. *AIChE J*. 2002;48:1631–1638.
33. Pain CC, Mansoorzadeh S, Oliverira CRE. A numerical investigation of bubbling gas-solid fluidized bed dynamics in 2-D geometries. *Powder Technol*. 2002;128:56–77.
34. Peirano B, Delloume V, Leckner B. Two- or three-dimensional simulations of turbulent gas-solid flows applied to fluidization. *Chem Eng Sci*. 2001;56:4787–4799.
35. Clift R, Grace JR. *Continuous bubbling and slugging*. London: Academic Press; 1985.
36. Geldart G. Types of gas fluidization. *Powder Technol*. 1973;7:285–292.
37. Dyakowski T, Edwards RB, Xie CG, Williams RA. Application of capacitance tomography to gas-solid flows. *Chem Eng Sci*. 1997; 52:2099–2110.
38. Wang HG, Yang WQ, Dyakowski D, Liu S. Study of bubbling and slugging fluidised beds by simulation and electrical capacitance tomography. *AIChE J*. 2006;52:3078–3087.
39. Lim CN, Gilbertson MA, Harrison AJL. Bubble distribution and behaviour in bubbling fluidised beds. *Chem Eng Sci*. 2007;62:56–69.
40. Werther J. Bubble growth in large diameter fluidized beds. In *Fluidization Technology*. Vol. 1. Kearnis DL, ed. Hemisphere, Washington DC. 1976;1:215–235.
41. Cohen A, Glicksman LR, Hughes RW. Semi-empirical prediction of bubble diameter in gas fluidized beds. *Int J of Multiphase Flow*. 1981; 7:101–113.
42. Horio M and Nonaka A. A generalized bubble diameter correlation for gas solid fluidized beds. *AIChE J*. 1987;33:1865–1872.
43. Yang WQ, Liu S. Electrical capacitance tomography with square sensor. *Electronics Letts*. 1999;35:295–296.
44. Pain CC. Mansoorzadeh S and Oliverira CRE. A study of bubbling and slugging fluidised beds using the two-fluid granular temperature model. *Int J Multiphase Flow*. 2001;27:527–551.
45. Chaplin G, Pugsley T, Van der Lee L, Kantzas A and Winters C. The dynamic calibration of an electrical capacitance tomography sensor applied to the fluidized bed drying of pharmaceutical granule. *Meas Sci Technol*. 2005;16:1281–1290.
46. Warsito W, Fan LS. ECT imaging of three-phase fluidized bed based on three-phase capacitance model. *Chem Eng Sci*. 2003;58:823–832.
47. Yang WQ, Chondronasios A, Nattrass S, Nguyen VT, Betting M, Ismail I, McCann H. Adaptive calibration of a capacitance tomography system for imaging water droplet distribution. *Flow Measurement and Instrumentation*. 2004;15:249–258.

Manuscript received Mar. 19, 2007, and revision received Nov. 19, 2007.